EES Catalysis

PAPER

View Article Online
View Journal

Cite this: DOI: 10.1039/d5ey00355e

Ultrafast interfacial charge transfer drives photocatalysis in heterojunctions between nitrogen-rich graphitic carbon nitride (g-C_3N_5) and amino-functionalized carbon quantum dots

Pratibha Saini,†*[a] Arindam Konar,†[ab] Ahmed Mansour,[a] Desirée Leistenschneider,[cd] Marius Hermesdorf,[c] Sarah Jasmin Finkelmeyer,[b] Martin Presselt,[bde] Martin Oschatz[cdf] and Benjamin Dietzek-Ivanšić[*abg]

Tailoring the electronic structure of polymeric carbon nitrides is key to advancing sustainable photocatalysis. Nitrogen-rich graphitic carbon nitride (g-C_3N_5) exhibits a narrower band gap, higher electron density, and stronger basicity than conventional g-C_3N_4, yet its photocatalytic activity remains limited by inefficient charge separation and fast recombination. Here, a 0D/2D heterojunction of amino-rich carbon quantum dots (AR-CQDs) anchored onto triazole-based g-C_3N_5 is reported *via* an ultrasound assisted hydrothermal strategy. The AR-CQDs induce N_{2C} vacancies and generate shallow interfacial states, enhancing charge separation and surface reactivity. The AR-CQDs/g-C_3N_5 heterojunction achieves a CO_2 reduction rate of 2653 ± 0.5 μmol h^{-1} g^{-1}, outperforming g-C_3N_5 and g-C_3N_4 by factors of 7 and 48, respectively. It exhibits a 3.4-fold increase (91 ± 2 μmol g^{-1}) in H_2 evolution over g-C_3N_5, with excellent stability across multiple cycles. Femtosecond transient absorption spectroscopy reveals an interfacial electron transfer on the picosecond timescale from photoexcited AR-CQDs to g-C_3N_5. This oxidative quenching process provides mechanistic evidence that ultrafast charge transfer underpins the enhanced photocatalytic performance. The combined structural engineering and spectroscopic insights establish AR-CQDs/g-C_3N_5 heterojunctions as a robust and metal-free platform, coupling defect/interface design with ultrafast charge dynamics for improved solar-to-fuel energy conversion systems.

Received 18th December 2025,
Accepted 3rd May 2026

DOI: 10.1039/d5ey00355e

rsc.li/eescatalysis

Broader context

Metal-free photocatalysts are increasingly attractive for sustainable energy conversion and environmental remediation, yet their practical performance remains constrained by inefficient charge separation and a limited mechanistic understanding of interfacial charge-transfer processes. Addressing these challenges requires not only new materials, but also fundamental insight into how interfacial electronic structure governs catalytic function. This work advances energy and environmental catalysis by establishing a direct, time-resolved link between ultrafast interfacial charge transfer and photocatalytic activity in a fully metal-free heterojunction composed of nitrogen-rich graphitic carbon nitride (g-C_3N_5) and amino-rich carbon quantum dots (AR-CQDs). Through the combined use of defect and interface engineering, quantitative photocatalytic evaluation, and femtosecond transient absorption spectroscopy, we reveal excitation-wavelength-dependent charge-transfer pathways that control charge-carrier lifetimes and reactivity under visible-light irradiation. Beyond performance improvement, this study provides a general, mechanism-anchored design principle for constructing earth-abundant, chemically robust photocatalysts in which interfacial charge regulation governs energy-relevant catalytic transformations. The insights reported here are broadly applicable to the rational design of next-generation metal-free catalytic systems for sustainable energy conversion and environmentally benign chemical transformations.

[a] *Institute for Physical Chemistry, Friedrich Schiller University Jena, Helmholtzweg 4, 07743 Jena, Germany. E-mail: sainip082@gmail.com*
[b] *Department Functional Interfaces, Leibniz Institute of Photonic Technology (Leibniz-IPHT), Albert-Einstein-Strasse 9, 07745 Jena, Germany*
[c] *Institute for Technical Chemistry and Environmental Chemistry, Friedrich Schiller University Jena, Philosophenweg 7a, 07743 Jena, Germany*
[d] *Center for Energy and Environmental Chemistry Jena (CEEC Jena), Friedrich Schiller University Jena, Philosophenweg 7a, 07743 Jena, Germany*
[e] *Sciclus GmbH & Co. KG, Moritz-von-Rohr-Str. 1a, 07745 Jena, Germany*
[f] *Helmholtz Institute for Polymers in Energy Applications Jena (HIPOLE Jena), Lessingstraße 12–14, 07743 Jena, Germany*
[g] *Leibniz Institute of Surface Engineering (Leibniz-IOM), Permoserstraße 15, 04318 Leipzig, Germany. E-mail: benjamin.dietzek-ivansic@iom-leipzig.de*
† P. S. and A. K. contributed equally to this work.

Introduction

Solar-to-chemical energy conversion using metal-free photocatalysts is a promising route towards sustainable fuel production and carbon management.[1–8] Among metal-free semiconductor photocatalysts, graphitic carbon nitride (g-C_3N_4) has emerged as a ''rising star'' owing to its chemical stability, visible-light absorption, non-toxicity, low-cost, and facile synthesis from nitrogen-rich organic precursors.[8–12] However, the relatively wide bandgap of g-C_3N_4 (2.7 eV) and rapid recombination of photoinduced charge carriers limit its photocatalytic efficiency.[13,14]

Recently, nitrogen-rich carbon nitrides (g-C_3N_5) with a 3 : 5 carbon : nitrogen stoichiometry have emerged.[15–17] The azo (–N═N–) and triazole moieties within the g-C_3N_5 framework extend the π-conjugation across the heptazine units,[16–20] narrow the materials band gap to *ca.* 1.9 eV, broaden the visible-light absorption, and reduce charge recombination while extending charge carrier mobility and lifetime.[16] Nonetheless, g-C_3N_5 still suffers from bulk recombination of photoinduced carriers, a low specific surface area, and a scarcity of active interfacial sites,[21–23] limiting its practical photocatalytic applications.[16–19] To this end, constructing heterojunctions with well-aligned band edges is particularly effective to enhance performance in light-driven reactions, as it promotes charge separation and suppresses recombination.[24,25] In particular, heterojunctions that pair 2D g-C_3N_4 with quantum dots (QDs), including materials like $AgVO_4$ and Bi_3TaO_7 show strong improvements.[26–28]

Carbon quantum dots (CQDs) offer a metal-free alternative with excellent dispersibility, photostability, biocompatibility, chemical inertness, large specific surface area, and low toxicity.[29–33] Abundant surface functional groups and conjugated π-structure in CQDs support interfacial coupling and efficient charge transfer through electrostatic interactions.[31–33] CQDs broaden light harvesting and – depending on the band alignment – serve as electron reservoirs or mediators, facilitating charge separation/transfer and prolonging carrier lifetimes.[33–36] Despite the progress with 0D/2D heterojunctions, metal-free combinations of N-rich g-C_3N_5 with CQDs remain scarcely explored for CO_2 reduction and H_2 evolution, even though such pairings are intrinsically sustainable and tunable.

Beyond catalytic performance alone, systematic spectroscopic insight into the charge carrier dynamics of g-C_3N_5-based heterojunctions remains limited,[37–41] and ultrafast studies on fully metal-free AR-CQDs/g-C_3N_5 systems are scarce. For example, few-layer C_3N_5 shows a 3.2-fold enhancement in photogenerated electron lifetimes compared to its bulk counterpart. Moreover, these lifetimes surpassed those of g-C_3N_4 by 3.7-fold, directly correlating with the superior photocatalytic activity.[37] Engineered states (*e.g.*, cyano groups) in high-crystalline C_3N_5, single-atom doping (Pt–N) in g-C_3N_5, and heteroatom motifs (C–S–C) in sulfur-doped g-C_3N_5 extend photogenerated carrier lifetimes and accelerate interfacial transfer, boosting H_2 evolution and nitric oxide (NO)/CO_2 conversions.[38–40] Heterojunctions such as g-C_3N_5/CdS further yield long-lived charge-separated states that persist into the nanosecond (ns) regime.[41]

Here a 0D/2D AR-CQDs/g-C_3N_5 heterojunction is prepared *via* a simple ultrasound-assisted hydrothermal route. Characterizations of phase, morphology, microstructure, and optical properties confirm successful integration and provide insight into this system's functionality. To uncover the mechanistic insights behind the improved photocatalytic activity, we combine band-edge analysis with femtosecond transient absorption (fs-TA) spectroscopy. We propose that CQD-derived carriers relax into a shallow interfacial state and inject into the g-C_3N_5 conduction band, a sequence that rationalizes suppressed recombination and sustained redox turnover. By uniting defect/interface engineering, ultrafast spectroscopy, and catalytic benchmarking in a fully metal-free platform, this study establishes a clear mechanistic link between picosecond interfacial charge transfer and performance gains, offering a general design principle for next-generation carbon-nitride photocatalysts.

Results and discussion

Synthesis and comprehensive structural, morphological, and electronic characterization of the synthesized photocatalysts

The AR-CQDs/g-C_3N_5 was synthesized through an ultrasound-assisted hydrothermal method from nitrogen-rich g-C_3N_5 (Scheme S1, see SI for synthesis of g-C_3N_5) and AR-CQDs (Fig. 1a). The effect of anchoring AR-CQDs[42–44] on the crystal structure of g-C_3N_5 was studied by X-ray powder diffraction (XRD) (Fig. 1b). Bulk g-C_3N_5 exhibits two typical diffraction reflexes of graphitic carbon nitride prepared *via* thermal condensation: a strong reflex originating from (002) plane at 27.5° (*d*-spacing 0.323 nm) associated with inter-planar stacking[45] and a weaker signal at 12.5° (*d*-spacing 0.704 nm) from the (100) plane arising from in-plane periodicity of triazole/triazines units in the g-C_3N_5.[41] No distinct diffraction signal associated with AR-CQDs[42] was detected in the XRD patterns of AR-CQDs/g-C_3N_5 due to the low content and amorphous/low crystallinity of AR-CQDs. Notably, AR-CQDs/g-C_3N_5 shows a sharper (100) reflex,[46] and a weak low-angle feature around 6.1°. Similar low-angle reflections have been reported for post-treated carbon nitride materials and were assigned to a (001)-type reflection, consistent with long-range stacking/periodicity changes.[47,48] Moreover, a change in the FWHM of the (002) peak is observed after processing, consistent with modified interlayer stacking and local structural reorganisation.[49a] (Fig. S1d and S1e, see SI). A slight shift of this peak from 27.57° to 27.38° is also observed (Fig. S1b, see SI), implying that the interlayer spacing of the graphite-like planes increased. This may be attributed to successful coupling of AR-CQDs with g-C_3N_5, accompanied by the introduction of oxygen-containing functionalities from the AR-CQDs.[49b] In addition, the attenuated total reflectance-Fourier transform infrared (ATR-FTIR) spectra of AR-CQDs/g-C_3N_5 is consistent with those of bulk g-C_3N_5. Any characteristic peaks stemming from AR-CQDs can't be observed, which may point to the low content of AR-CQDs (Fig. 1c). To verify that the amino functionalities of AR-CQDs are retained under the hydrothermal conditions used for

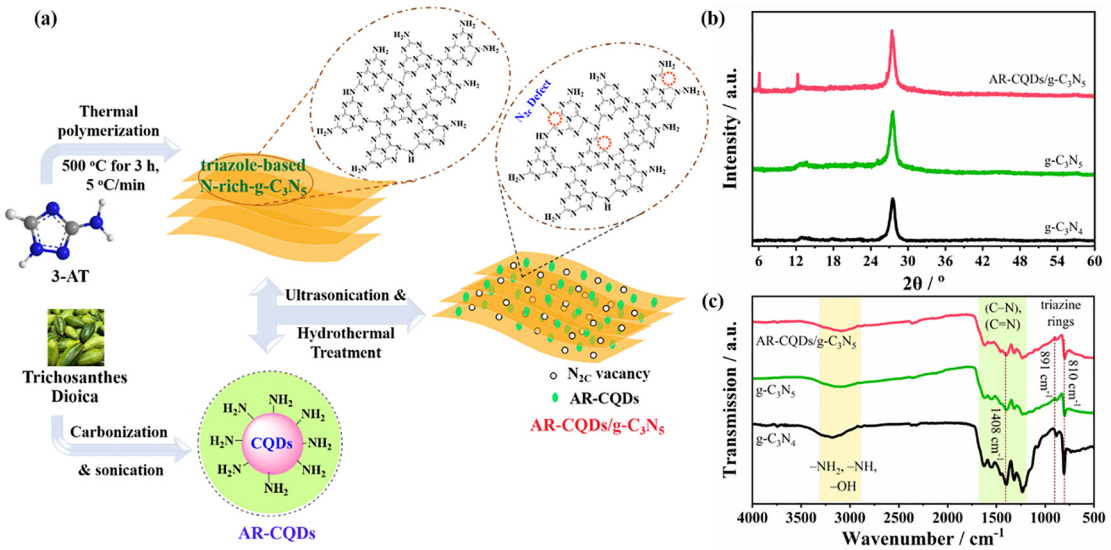

Fig. 1 (a) Synthesis process of AR-CQDs/g-C_3N_5. (b) XRD patterns and (c) FT-IR spectra of g-C_3N_4, g-C_3N_5, and AR-CQDs/g-C_3N_5.

heterojunction preparation, high-resolution N 1s XPS spectra were recorded before and after treatment, confirming the persistence of the $-NH_2$ associated signal (Fig. S1f–g). The broad band at 3000–3400 cm^{-1} stems from stretching vibrations of uncondensed $-NH_2$ or surface-adsorbed water molecules (O–H groups). Bands in 1700–1200 cm^{-1} region correspond to stretching vibrations of the heterocyclic C–N unit (triazine units). Notably, conventional g-C_3N_4 exhibits strong absorption peaks at 891 cm^{-1} and 810 cm^{-1}, which are characteristic of condensed C–N heterocycles in the triazine framework. However, in g-C_3N_5 and AR-CQDs/g-C_3N_5, these peaks show reduced intensity, suggesting a lower presence of C–N bonds in the triazole-based N-rich g-C_3N_5 materials.[50] Moreover, a peak at 1408 cm^{-1} evidences N–N stretching in triazole-based moieties.[51] These features confirm the coexistence of triazole and triazine groups in the carbon nitride network.[52]

To elucidate the surface morphology and integration of AR-CQDs within g-C_3N_5, field emission scanning electron microscopy (FE-SEM) and transmission electron microscopy (TEM) analyses were performed (Fig. 2a–f). FE-SEM and TEM images of bulk g-C_3N_5 (Fig. 2a and c) and TEM image of conventional g-C_3N_4 (Fig. S2a, see SI) present a smooth surface and tight rock-shaped lamellar structure, while FE-SEM image of AR-CQDs/g-C_3N_5 displays a rough surface and porous structure (Fig. 2b). The TEM image of AR-CQDs/g-C_3N_5 (Fig. 2d) shows a porous morphology with voids, indicating the presence of mesostructured features, which is further corroborated by increase in the specific surface area from 4 to 13 m^2 g^{-1} (Fig. S2b, see SI). The distribution of AR-CQDs within the matrix of g-C_3N_5 can be observed in the TEM images (Fig. 2e and f) of AR-CQDs/g-C_3N_5 with an average particle size of 2.6 ± 0.4 nm.

The energy-dispersive X-ray (EDX) analysis of the synthesized photocatalysts was conducted to determine their chemical composition. As anticipated, the EDX spectra of AR-CQDs/g-C_3N_5 (Fig. 2j), g-C_3N_5 (Fig. S3e–h, see SI) and g-C_3N_4 (Fig. S3a–d, see SI) revealed only the presence of C, N, and O elements, confirming the purity of the samples. AR-CQDs/g-C_3N_5 displays a notably higher concentration of oxygen (Fig. 2j), likely attributed to functional groups such as amide, hydroxyl, carbonyl, and carboxyl in AR-CQDs. These results are consistent with the successful incorporation and homogeneous distribution of oxygen-rich carbon domains within the g-C_3N_5 matrix. Furthermore, elemental mappings (Fig. 2g–i) clearly demonstrate even spatial distribution of C and N elements across AR-CQDs/g-C_3N_5.

To probe the chemical and electronic changes induced by integrating AR-CQDs into g-C_3N_5, we employed X-ray photoelectron spectroscopy (XPS), electron paramagnetic resonance (EPR), and solid-state NMR spectroscopy. The XP spectra of g-C_3N_4, g-C_3N_5, and AR-CQDs/g-C_3N_5 are illustrated in Fig. S4 and S5 (see SI), and Fig. 3a–d, respectively, with quantitative peak positions and relative contributions summarized in Table S1 (N 1s) and Table S2 (C 1s) (see SI).

High-resolution N 1s XP spectra of g-C_3N_5 reveals five characteristic peaks, corresponding to pyridinic N (N_{2C}; 398.4 eV), N–$(C)_3$ (N_{3C}; 399.1 eV), N–H_x/N═CH–N (401.0 eV), pyrrolic N (400.6 eV), and π–π* excitation in the heterocycle (404.3 eV). The distinct pyrrolic N peak of g-C_3N_5 (400.6 eV),[45] (Fig. S5b and Table S1, see SI), absent in g-C_3N_4 (Fig. S4b, see SI), supports the successful formation of triazole ring-based, nitrogen-rich g-C_3N_5, in agreement with FT-IR results (Fig. 1c, *vide supra*). The similar feature with distinct pyrrolic N peak (399.9 eV) can be observed for AR-CQDs/g-C_3N_5 (Fig. 3b and Table S1, see SI). Notably, the N_2C/N_3C peak-area ratio decreases from 4.52 for pristine g-C_3N_5 to 2.39 for AR-CQDs/g-C_3N_5 (Table S1, see SI), consistent with AR-CQDs-assisted modification of nitrogen coordination environments during ultrasonic/hydrothermal processing. This behavior likely arises

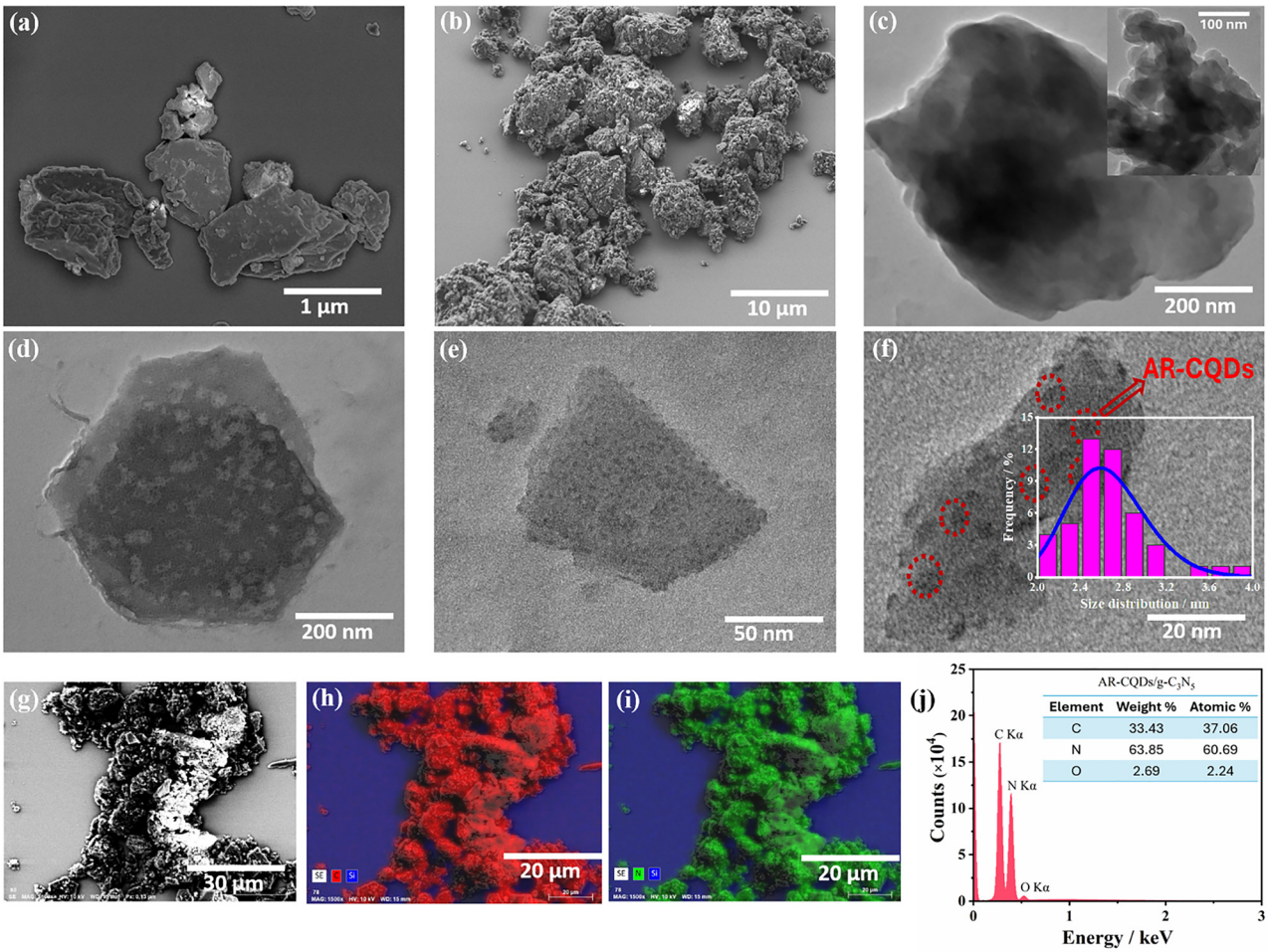

Fig. 2 FE-SEM images of (a) bulk g-C_3N_5 and (b) AR-CQDs/g-C_3N_5. (c) TEM images of bulk g-C_3N_5 and (d)–(f) AR-CQDs/g-C_3N_5. The insert spectra in (f) shows the size distribution histogram of AR-CQDs/g-C_3N_5. (g)–(i) Energy dispersive X-ray spectroscopy (EDX) mapping images of AR-CQDs/g-C_3N_5. (j) EDX spectrum of AR-CQDs/g-C_3N_5 (inset: elemental composition).

from interfacial interactions between the functionalized AR-CQDs surface and the g-C_3N_5 framework, which promote local restructuring of the more labile N_2C sites. As a result, defect-like features preferentially involve two-coordinated N_2C species, in line with their lower bonding stability compared to N_3C.[53] The high-resolution C 1s spectrum of g-C_3N_5 (Fig. S5a and Table S2, see SI) has four peaks at 288.0 eV, 284.6 eV, 286.0 eV, and 293.3 eV, corresponding to N═C–N_2 coordination in the triazole-based N-rich g-C_3N_5 framework, C–C/C═C in graphitic carbon species, C–NH_x at the edges of heptazine units, and π–π* excitation in the heterocycle, respectively. Upon AR-CQDs incorporation, the contribution around 286.0 eV becomes more pronounced for AR-CQDs/g-C_3N_5 (Fig. 3a) and is assigned to C–NH_x/C–O species, indicating the emergence of oxygenated interfacial carbon environments after hybridization. In combination with the O 1s evolution (Fig. 3c), these changes support covalent anchoring *via* oxygen-containing interfacial linkages between g-C_3N_5 and AR-CQDs.[49b],54 The high-resolution O 1s spectrum (Fig. 3c) is deconvoluted into components centred at 530.9 eV (C═O), 532.1 eV (C–O), and 533.0 eV (C–O–C/C–OH).[43,44,49b] The XP survey spectra confirm the presence of C, N, and O in both g-C_3N_5 (Fig. S5d, see SI) and AR-CQDs/g-C_3N_5 (Fig. S5e).

The EPR and solid-state NMR spectroscopy provided additional evidence for N_{2C} vacancies in AR-CQDs/g-C_3N_5. EPR spectra (Fig. 3e) exhibit a single Lorentzian line at around 3519 G, with a *g*-value of 2.0042, for all three samples, which is commonly assigned to unpaired electrons in π-conjugated carbon nitride frameworks. The signal intensity is stronger in g-C_3N_5 than g-C_3N_4, reflecting increased electron mobility and π-delocalization in N-rich g-C_3N_5 framework. A substantial increase in EPR intensity in AR-CQDs/g-C_3N_5 is attributed to the combined effects of N_{2C} vacancy formation, resulting in excess electrons redistributed to adjacent carbon atoms, leading to more unpaired electrons and strong π–π interactions at the AR-CQDs/g-C_3N_5 interface. Solid-state ^{13}C NMR of g-C_3N_5 and AR-CQDs/g-C_3N_5 (Fig. 3f) shows an intense peak at a chemical shift of *ca.* 164 ppm, associated with sp^2 C-atoms adjacent to three N-atoms and attached to the end groups, and *ca.* 156 ppm, assigned to sp^2 carbon atoms in N═C–N bonds, consistent with heptazine rings in both materials. Nevertheless, these two peaks for AR-CQDs/g-C_3N_5 separately shift downfield

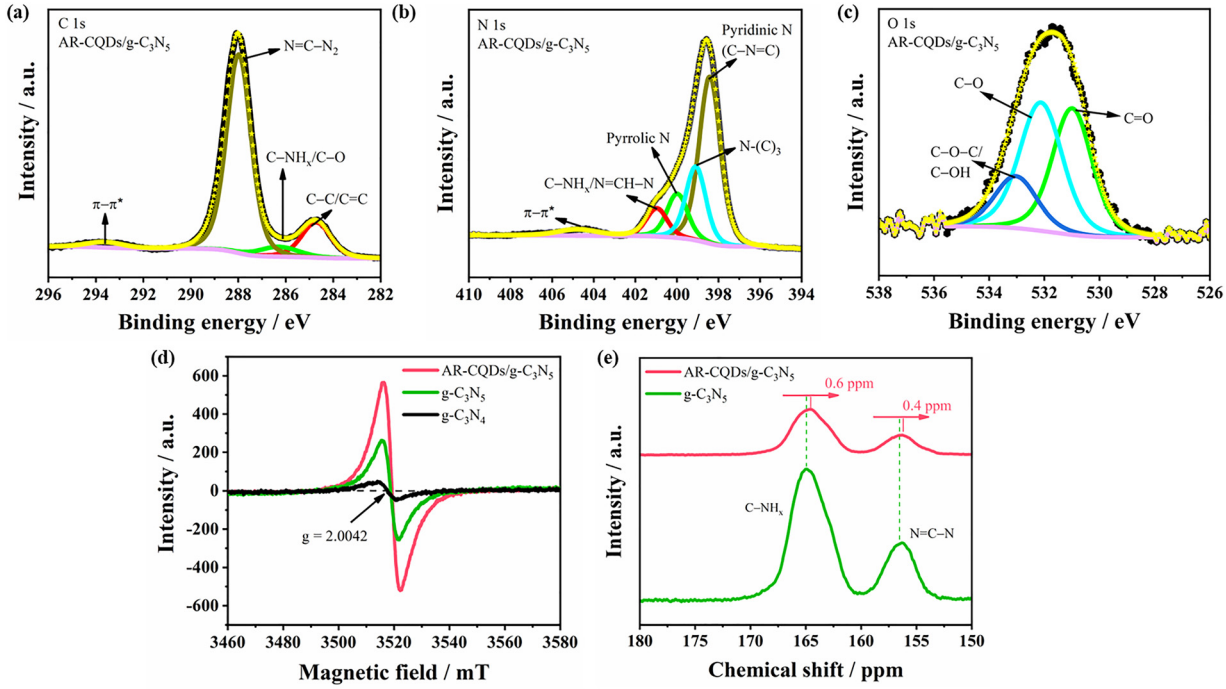

Fig. 3 High-resolution XP spectra of AR-CQDs/g-C_3N_5: (a) C 1s, (b) N 1s, and (c) O 1s. (d) EPR spectra of g-C_3N_4, g-C_3N_5 and AR-CQDs/g-C_3N_5. (e) Solid-state NMR spectra of g-C_3N_5 and AR-CQDs/g-C_3N_5.

by 0.6 and 0.4 ppm, indicating increased electron density around these carbons upon N_{2C} vacancy generation after AR-CQDs anchoring. Additionally, the shoulder at *ca.* 154 ppm in AR-CQDs/g-C_3N_5 suggests minor imperfections in the conjugated aromatic ring network, attributable to the presence of N_{2C} vacancies.[55,56]

Electronic band structure and energy-level alignment of the synthesized photocatalysts

To investigate the electronic structure of AR-CQDs/g-C_3N_5 UV-vis diffuse reflectance spectroscopy (DRS) is combined with valence band (VB) XPS. Compared to traditional g-C_3N_4, the bulk g-C_3N_5 and AR-CQDs/g-C_3N_5 exhibit significantly enhanced visible light absorption, with absorption edges at *ca.* 668 nm and 612 nm, respectively, due to overlap of N 2p orbitals that expands the π-conjugated aromatic systems (Fig. 4a). The red-shifted absorption tail extending to *ca.* 727 nm in AR-CQDs/g-C_3N_5 arises from N_{2C}-vacancy-induced mid-gap states (MGSs) overlapping with the conduction band (CB).[57] The band structure of the samples was analyzed using VB-XPS (Fig. 4b), placing the VB edges at 1.62 eV for g-C_3N_5 and 1.71 eV for AR-CQDs/g-C_3N_5. Using the equation, $E_g = E_{VB} - E_{CB}$, where E_g, E_{VB}, and E_{CB} represent band gap energy, VB potential, and CB potential, respectively, the CB potentials are estimated as −0.75 eV for AR-CQDs/g-C_3N_5 and −0.47 eV for bulk g-C_3N_5. This negative shift of the CB potential in AR-CQDs/g-C_3N_5 enhances the thermodynamic driving force for light-driven redox reactions, particularly CO_2 photoreduction and H_2 evolution. The combination of a more negative CB, a slightly more positive VB, and the presence of MGSs enhances the overall redox capacity of AR-CQDs/g-C_3N_5.[58] The band gap energies of the synthesized samples, calculated *via* Tauc plots (Fig. 4c and Table S3, see SI), reveal an increase of the band gap for AR-CQDs/g-C_3N_5 (2.46 eV) compared to pristine g-C_3N_5 (2.09 eV). This apparent widening in AR-CQDs/g-C_3N_5 reflects electronic reconstruction and band-edge shifting upon vacancy formation, while the concomitant MGSs introduce additional low-energy absorption pathways and facilitate interfacial charge transfer.

Evaluation of photocatalytic performance

The photocatalytic activity of AR-CQDs/g-C_3N_5 has been evaluated for both CO_2 photoreduction and H_2 evolution under visible-light irradiation.

The CB edges of g-C_3N_5 and AR-CQDs/g-C_3N_5 lie above CO_2/acetaldehyde (CH_3CHO) redox potential (−0.36 eV), confirming their general thermodynamic ability for CO_2 reduction. A liquid-phase CO_2 photocatalytic system was used, containing 5 mg of a photocatalyst (Fig. S7a, see SI), a solvent, and a sacrificial donor. A mixture of acetonitrile and water in 4 : 1 volume ratio was chosen as solvent, where acetonitrile helped dissolve gaseous CO_2, and water provided protons needed for the reaction. Under blue-light irradiation, AR-CQDs/g-C_3N_5 achieved an outstanding CH_3CHO generation rate of 2653 ± 0.5 μmol h^{-1} g^{-1}, showing a nearly 7-fold increase over pristine g-C_3N_5 (380 ± 0.5 μmol h^{-1} g^{-1}) and a 48-fold improvement compared to traditional g-C_3N_4 (55.3 ± 0.5 μmol h^{-1} g^{-1}) (Fig. 5a). The enhancement arises from the synergistic effect of AR-CQDs anchoring and N_{2C} vacancy formation, which jointly promote charge separation and interfacial redox activity. CH_3CHO generation

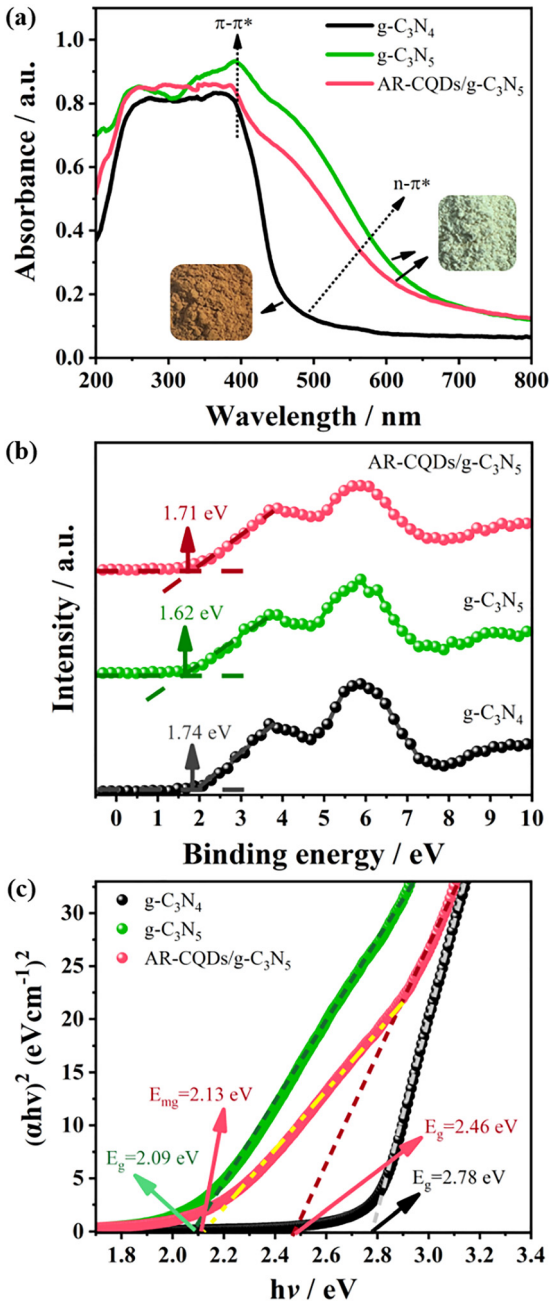

Fig. 4 Optical properties of g-C_3N_4, g-C_3N_5 and AR-CQDs/g-C_3N_5: (a) UV-vis DRS spectra. (b) VB-XP spectra. (c) Tauc plots for the determination of bandgap and mid-gap states.

rapidly improved with illumination time (Fig. 5c), reaching an average CH_3CHO production rate of 21.2 mmol h^{-1} g^{-1} over 8 h. AR-CQDs/g-C_3N_5 showcased exhibited high selectivity toward CO_2 reduction to CH_3CHO, and calibrated GC and GC–MS analyses identified acetaldehyde as the dominant product under the applied conditions. While most reported g-C_3N_5-based photocatalysts predominantly yield C1 products, theoretical studies suggest that multi-carbon product formation is not primarily excluded under suitable conditions, supporting the feasibility of CH_3CHO generation observed here.[58]

The CH_3CHO product formation was confirmed through gas chromatography (GC) (S7b, see SI) and ^1H NMR spectroscopy (Fig. S8, see SI). Side-products such as H_2, O_2, and CO remained negligible.

To identify the source of CH_3CHO formation (Fig. 5b), it was verified that no products were observed when CO_2 reduction experiments were carried in the absence of a photocatalyst, without light, and/or in an N_2 atmosphere. These results linked enhanced CH_3CHO production to the photocatalytic reduction of CO_2, driven by the photocatalyst and light. The photocatalytic activity decreased notably without a hole scavenger, underscoring the role of the sacrificial donor in minimizing exciton recombination and facilitating multielectron CO_2 photoreduction into CH_3CHO. Isotope labeling using $^{13}CO_2$ further confirmed that the carbon source originated from CO_2, as characteristic peaks at m/z = 30 and 46 corresponding to formyl cation ($^{13}CHO^+$) and molecular ion ($^{13}CH_3{}^{13}CHO^+$) were detected in the GC-mass spectrum (GC-MS) (Fig. 5d). The performance of AR-CQDs/g-C_3N_5 surpasses other literature-known photocatalysts yielding CH_3CHO as a main product (Table S4, see SI), demonstrating that defect/interface engineering can deliver efficient and selective CO_2-to-CH_3CHO conversion without metal cocatalysts. CH_3CHO is an energy-dense valuable liquid-phase product and a key intermediate in the synthesis of industrial chemicals including acetic acid, ethanol, and ethyl acetate. These aspects highlight the relevance of selective CH_3CHO formation for potential downstream chemical applications, indicating that AR-CQDs/g-C_3N_5 may offer practical advantages under suitable conditions.

AR-CQDs/g-C_3N_5 also exhibited excellent photocatalytic H_2 evolution in an aqueous triethanolamine solution under blue-light irradiation. Under the optimized reaction conditions used in this work (5 mg catalyst; aqueous TEOA solution; blue-light irradiation), AR-CQDs/g-C_3N_5 produced 91 ± 2 μmol g^{-1} of H_2 within 6 h, which is 3.4-fold higher than pristine g-C_3N_5 (26.8 ± 2 μmol g^{-1}) and about 15-fold higher than g-C_3N_4 (6.2 ± 0.5 μmol g^{-1}) (Fig. 5f). Control experiments confirmed negligible H_2 evolution in the absence of light or catalyst.

The parallel trends in CO_2 reduction and H_2 evolution clearly highlight the cooperative roles of AR-CQDs and N_{2C} vacancies in the g-C_3N_5 framework. Photocatalytic cycling tests of AR-CQDs/g-C_3N_5 demonstrated structural and catalytic stability over five consecutive cycles for both CO_2 reduction and H_2 evolution (Fig. 5e and Fig. S9, see SI). XRD patterns (Fig. S10a, see SI) and FT-IR spectra (Fig. S10b, see SI) of AR-CQDs/g-C_3N_5 show no significant differences before and after catalysis, indicating the photocatalyst's structural integrity. The observed stability likely arises from the close interfacial contact between AR-CQDs and g-C_3N_5, which can support effective charge communication within the heterostructure.

Charge-transfer and probable reaction mechanism

To examine the charge carrier dynamics in AR-CQDs/g-C_3N_5, transient photocurrent responses, electrochemical impedance spectroscopy (EIS), and transient absorption spectroscopy (TAS) were recorded.

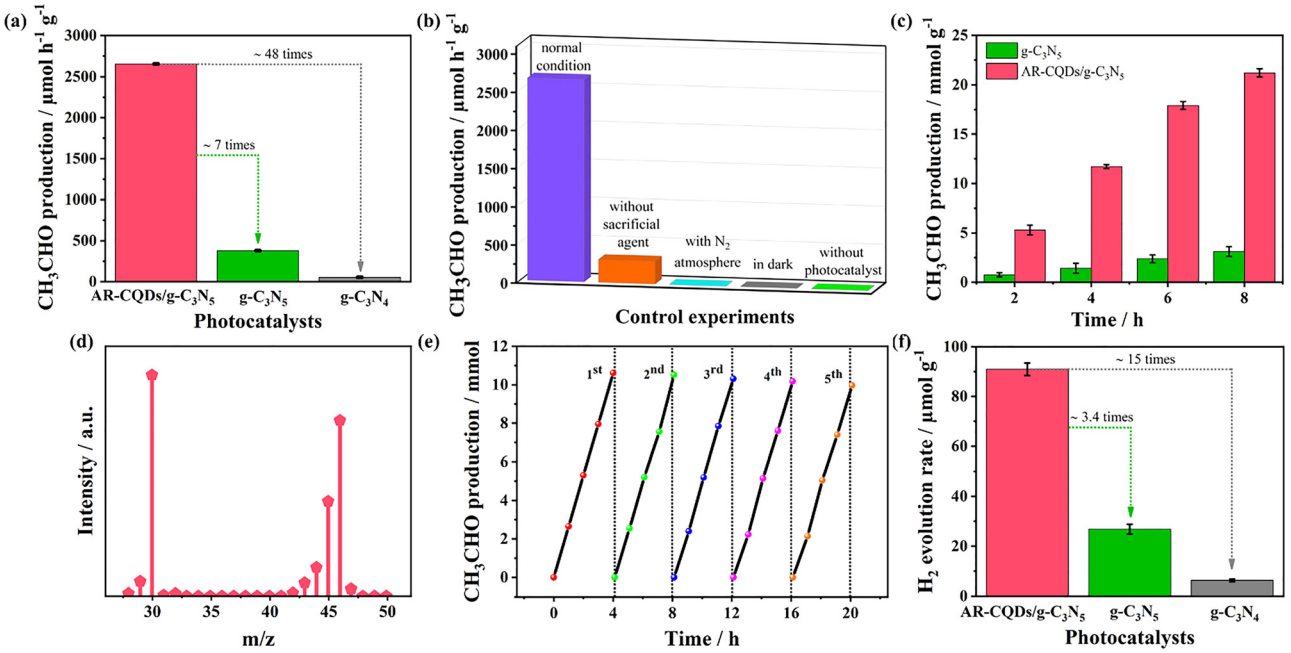

Fig. 5 Evaluation of photocatalytic CO_2 reduction. (a) Comparison of CH_3CHO production among all synthesized samples under optimized conditions (5 mg catalyst; MeCN/H_2O = 4 : 1; blue-light irradiation; further details in the SI). (b) Control experiments demonstrating CO_2 reduction under varying conditions. (c) Time-dependent CH_3CHO production during an 8-hour photocatalytic test. (d) Mass spectra derived from GC–MS analysis confirming the formation of $^{13}CH_3{}^{13}CHO$ (inset: corresponding GC chromatogram). (e) Stability assessment through cycling experiments using AR-CQDs/g-C_3N_5. (f) Photocatalytic H_2 production rates of the synthesized samples.

Fig. 6a depicts the transient photocurrent responses of all catalysts during multiple on–off light cycles. AR-CQDs/g-C_3N_5 demonstrates a higher photocurrent density (around 0.70 μA cm^{-2}) compared to pristine g-C_3N_5 (around 0.45 μA cm^{-2}) and traditional g-C_3N_4 (around 0.24 μA cm^{-2}). The enhanced photocurrent density reflects a more efficient electron transfer in AR-CQDs/g-C_3N_5 and is in line with the improved photocatalytic performance of the material. The simultaneous anchoring of AR-CQDs and N_{2C} vacancy formation accelerate electron transfer to catalytic active sites, while AR-CQDs/g-C_3N_5 regulates interfacial charge transport and suppresses recombination.[59] This is further supported by EIS measurements (Fig. 6b). The Nyquist plot for AR-CQDs/g-C_3N_5 exhibits a smaller semicircle radius compared to both traditional g-C_3N_4 and pristine g-C_3N_5, indicating lower charge-transfer resistance and faster internal charge transfer. This contributes to improved separation of photoinduced electron–hole pairs in AR-CQDs/g-C_3N_5. Together, these results evidence enhanced electron conductivity and interfacial charge transfer in AR-CQDs/g-C_3N_5.

To relate the observed photocurrents to underlying photoinduced processes, we first consider the absorption spectrum of AR-CQDs/g-C_3N_5, which contains features of both pristine g-C_3N_5 and AR-CQDs, maintaining strong UV absorption between *ca.* 200–350 nm and significant visible-light absorption (Fig. S11a, see SI). This implies that the intrinsic optical properties of g-C_3N_5 are not perturbed by the AR-CQDs anchoring in AR-CQDs/g-C_3N_5. Surface-sensitive photothermal deflection spectroscopy (PDS) results (Fig. S12, see SI) on drop-casted thin films of g-C_3N_5, AR-CQDs, and AR-CQDs/g-C_3N_5 closely resemble to their UV-vis absorption profiles in well-dispersed aqueous suspension, confirming that the optical modifications induced by AR-CQDs integration are consistent throughout the film and accessible at the interface. Photoluminescence (PL) further supports this picture: upon excitation at 400 nm, g-C_3N_5 emits at 435 nm,[21] while AR-CQDs/g-C_3N_5 shows a slight red-shift (440 nm; Fig. S11b–d, see SI), consistent with slightly altered energetics of the emissive state. AR-CQDs exhibit broad, excitation-dependent PL (Fig. S11e, see SI) from surface states and dominate at shorter excitation wavelengths (320–380 nm).[60–66] The weaker PL of AR-CQDs, upon excitation at 400–500 nm, reflects features of both g-C_3N_5 and AR-CQDs/g-C_3N_5. At longer excitation wavelengths, where AR-CQDs absorption is minimal, the PL of AR-CQDs/g-C_3N_5 closely mirrors that of g-C_3N_5, indicating that the observed PL originates from g-C_3N_5. A comprehensive discussion of the steady-state spectroscopy and PDS measurements can be found in the SI (see Note S1 and Fig. S11 and S12 in the SI).

Guided by the steady-state spectroscopy, femtosecond (fs) TAS resolves the interfacial charge carrier dynamics. Upon photoexcitation of pristine g-C_3N_5 at 400 nm, a ground-state bleach (GSB) between 430 and 680 nm appears (Fig. 6c). The bleach gradually recovers with increasing delay time. Beyond 680 nm, a comparably weak and broad excited-state absorption (ESA) emerges, indicating the presence of photogenerated charge carriers, *e.g.*, CB electrons or electrons localized on shallow trap states or MGSs.[67,68] The interaction of AR-CQDs with g-C_3N_5 in AR-CQDs/g-C_3N_5 induces spectral changes in the differential absorption spectra (Fig. 6d). While the GSB is still

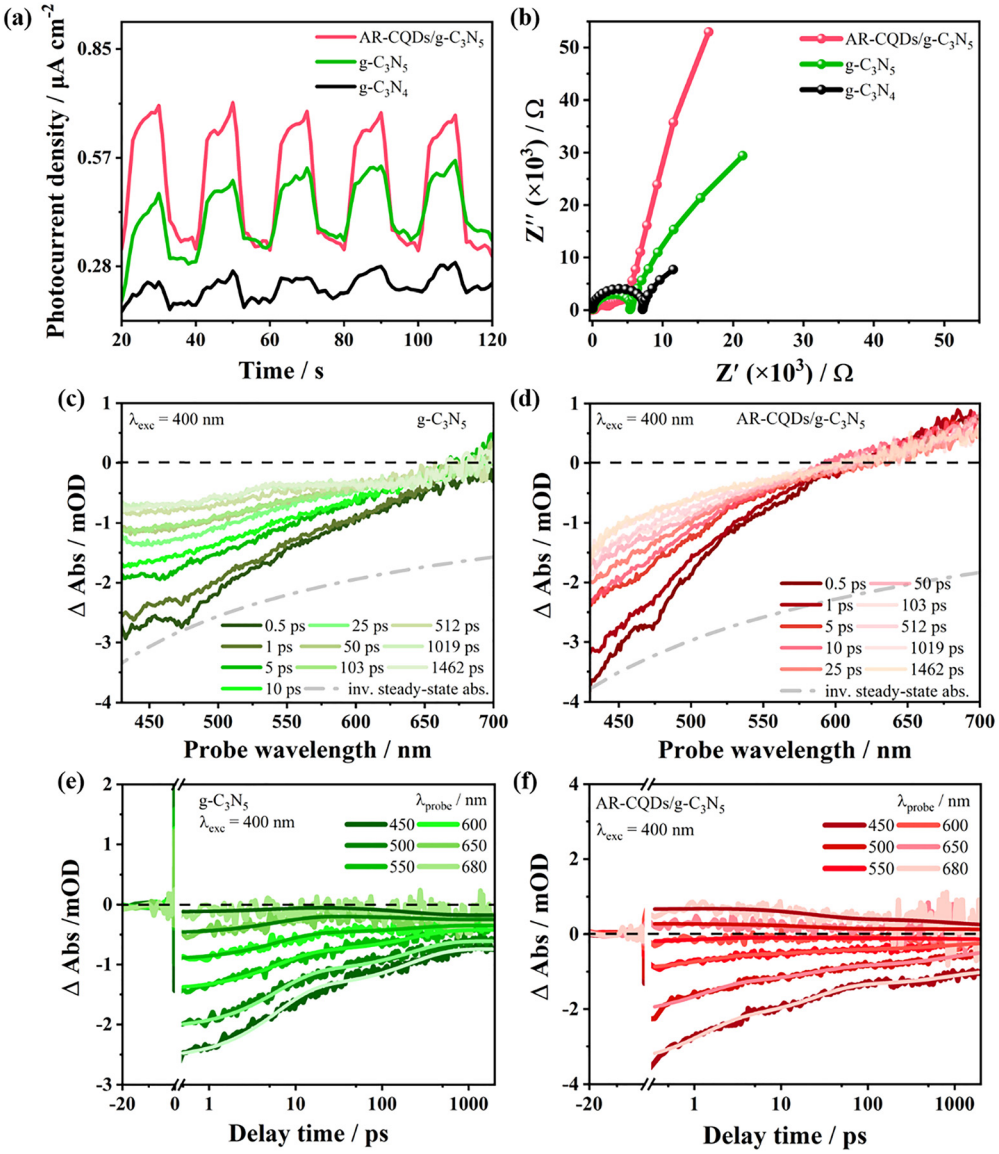

Fig. 6 (a) Visible light transient photocurrent response and (b) EIS spectra of g-C_3N_4, g-C_3N_5, and AR-CQDs/g-C_3N_5. Femtosecond (fs) transient absorption (TA) spectra of (c) g-C_3N_5 and (d) AR-CQDs/g-C_3N_5 (0.5 mg mL^{-1} concentration) at 400 nm excitation. Inverted steady-state absorption spectra are represented with dotted lines along with the TA spectra. fs-TA decay kinetics of (e) g-C_3N_5 and (f) AR-CQDs/g-C_3N_5. The solid lines within the TA data represent corresponding global fits.

pronounced in AR-CQDs/g-C_3N_5, the zero crossing between GSB and ESA is blue-shifted compared to that of g-C_3N_5. We propose that this spectral shift is associated with interfacial charge transfer between the photoexcited AR-CQDs and g-C_3N_5, that is otherwise absent in the individual components under identical excitation conditions. However, the fs-TA spectra of AR-CQDs at 400 nm excitation (Fig. 7a) reveal an ESA feature extending broadly into the red spectral region. The ESA signal gradually diminishes with increasing delay times but remains positive within the sub-ns time scale, indicating that the broad ESA band emerges from persistent charge carriers populating various trap states, possibly associated with surface functionalities and defects typical of CQDs.[61,62] Considering the substantial ESA observed for the AR-CQDs, it is critical to ascertain whether the TA spectra of AR-CQDs/g-C_3N_5 truly reflect interfacial electron transfer or merely a spectral superposition of individual AR-CQDs and g-C_3N_5 features.

To address this, we subtracted the TA spectra of g-C_3N_5 from the TA spectra of AR-CQDs/g-C_3N_5. The resultant spectra simulate the AR-CQDs contributions to the overall light-induced dynamics of AR-CQDs/g-C_3N_5. Comparing this simulated TA spectrum with independently measured AR-CQDs spectra at very early delay times (500 fs, 1 ps, and 1.5 ps) indicates excellent spectral overlap within the probe wavelength range 520–700 nm (Fig. 7b). This points to the fact that, initially excitations in the AR-CQDs and g-C_3N_5 parts of the heterojunction decay independently. However, at delay times >1.5 ps, the spectra simulating the AR-CQDs contributions to AR-CQDs/g-C_3N_5 and the

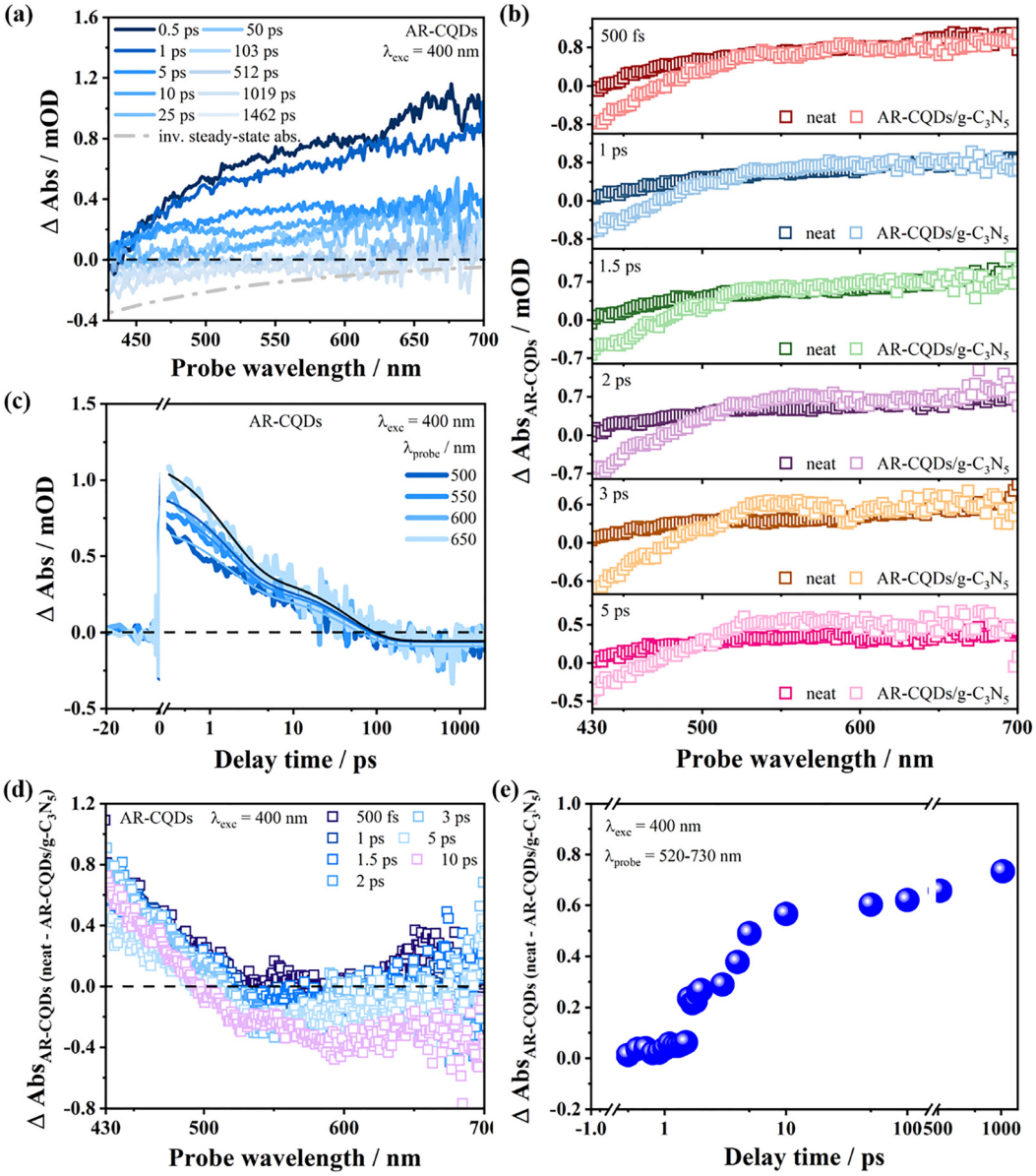

Fig. 7 (a) fs-TA spectra of AR-CQDs (concentration 2 mg mL^{-1}) at different delay times upon 400 nm excitation. Inverted steady-state absorption spectra are represented with dotted lines along with the TA spectra. (b) fs-TA spectra of AR-CQDs (represented as neat) and AR-CQDs contribution (by subtracting TA spectra of g-C_3N_5 from that of AR-CQDs/g-C_3N_5) within AR-CQDs/g-C_3N_5 (represented as heterojunction) at selected early delay times within 500 fs and 5 ps. (c) fs-TA decay kinetic traces of AR-CQDS upon 400 nm excitation. The solid lines represent the corresponding global fits. (d) Differential fs-TA spectra of AR-CQDs (neat) and AR-CQDs contribution (by subtracting TA spectra of g-C_3N_5 from that of AR-CQDs/g-C_3N_5) at selected time delays upon 400 nm excitation. (e) Kinetics of absolute absorbance differences between fs-TA data of AR-CQDs (neat) and AR-CQDs contribution (by subtracting TA spectra of g-C_3N_5 from that of AR-CQDs/g-C_3N_5), spectrally integrated between 520–700 nm at different delay times.

independently measured AR-CQDs start to deviate from each other. This indicates that electronic interactions occur in AR-CQDs/g-C_3N_5 and lead to different excited-state relaxation pathways, *i.e.*, by interfacial electron transfer between the two materials in the heterojunction. To estimate the temporal evolution of the differences between the TA spectra of AR-CQDs and the spectra simulating the AR-CQD's contribution in AR-CQDs/g-C_3N_5 (Fig. 7d), we integrate the absolute differences between measured and simulated AR-CQDs spectra between 520 and 700 nm at each delay time. At early times, the integral remains negligible, but beyond *ca.* 1.5 ps, a sharp rise in the integral can be observed (Fig. 7e). This indicates the onset of electron transfer between the AR-CQDs and g-C_3N_5 in the heterojunction.

A global biexponential fit to the fs-TA of g-C_3N_5 yields two characteristic time constants: $\tau_1 \approx 6$ ps and $\tau_2 \approx 214$ ps (Fig. 6e). The fast component ($\tau_1 \approx 6$ ps) corresponds to the material-intrinsic exciton decay, likely involving rapid trapping

in shallow defect states.[69] The longer component ($\tau_2 \approx 214$ ps) represents carrier recombination mediated by intrinsic mid-gap defect states, such as nitrogen vacancies naturally present in the pristine g-C_3N_5. The AR-CQDs, when excited at 400 nm and probed across the ESA range, feature a global biexponential kinetics with a fast (2.1 ps) and a slower decay component (47.4 ps; Fig. 7c). The initial fast component corresponds to internal relaxation processes, including vibrational relaxation and energy redistribution and exciton cooling within the AR-CQDs. The slower component is attributed to non-radiative recombination or trapping processes involving surface or defect states.[70] Global analysis of the TA data obtained for AR-CQDs/g-C_3N_5 requires a triexponential decay function, yielding the characteristic time constants: $\tau_1 \approx 1.8$ ps, $\tau_2 \approx 24$ ps, and $\tau_3 \approx 982$ ps (Fig. 6f). The fastest component observed in AR-CQDs/g-C_3N_5 ($\tau_1 \approx 1.8$ ps) is not present in either pristine g-C_3N_5 or AR-CQDs and – in line with the analysis of the differential spectra (*vide supra*) (Fig. 7b, d, and e) – is attributed to rapid interfacial electron transfer from photoexcited AR-CQDs to g-C_3N_5, giving rise to a distinct interfacial charge-separated state. While the timescale of this component (1.8 ps) overlaps with the fast AR-CQDs-internal relaxation (2.1 ps), the processes differ in spectral behavior. This becomes evident from the decay-associated spectra (DAS) obtained from the global fits (Fig. S13, see SI): 1.8 ps DAS of AR-CQDs/g-C_3N_5 exhibits a GSB in 430–610 nm region that crosses over into positive absorption toward longer wavelengths, whereas the 2.1 ps DAS of AR-CQDs is a broad, positive ESA. In AR-CQDs, the ESA band decay gradually without noticeable spectral changes (Fig. 7a and c), whereas, in AR-CQDs/g-C_3N_5, AR-CQDs contribution starts to deviate from the neat AR-CQDs spectrum after 1.5 ps (Fig. 7b, d, and e) and the bleach/ESA crossing shifts to shorter wavelength (Fig. 6d). This spectral divergence in AR-CQDs/g-C_3N_5 is consistent with charge leaving the AR-CQDs and being trapped in g-C_3N_5 and strongly supports the assignment of the 1.8 ps component as interfacial electron transfer rather than internal excited-state relaxation within the AR-CQDs. Following initial ultrafast electron injection, we associate the intermediate decay component ($\tau_2 \approx 24$ ps) in AR-CQDs/g-C_3N_5 to hot carrier relaxation and charge trapping. The latter process likely involves localized N_{2C} vacancy defect sites, which constitute MGSs within the g-C_3N_5 structure. The long-lived sub-ns component ($\tau_3 \approx 982$ ps) reflects the lifetime of electrons trapped deeply in these localized mid-gap defect states and their eventual recombination loss. The fs-TA data might be correlated to the chemical structure of the heterojunction: anchoring of AR-CQDs to the g-C_3N_5 opens an ultrafast electron transfer channel (1.8 ps) from AR-CQDs to g-C_3N_5. At the same time mid-bandgap states associated with N_{2C}-vacancies act as relay/trap states that capture the injected electrons (24 ps), while the trapped-electron population exhibits a lifetime of about 982 ps before eventual recombination loss. Thus, the interface governs charge separation, whereas the defect states stabilize the separated electrons, together providing the microscopic basis for the enhanced photocatalytic performance.

We further studied the system with fs-TAS upon excitation at 320 nm and 480 nm. The fs-TA measurements of AR-CQDs upon 320 nm excitation reveal broad ESA band across 450–650 nm and biexponential relaxation behavior, reflecting rapid internal conversion (300 fs) followed by carrier trapping (*ca.* 27 ps; Fig. S14, see SI). Both g-C_3N_5 and AR-CQDs/g-C_3N_5, under the same excitation, show nearly identical TA line shapes, featuring a GSB between 370 and 600 nm accompanied by an ESA beyond *ca.* 600 nm. Their kinetics follow biexponential decay with the characteristic time constants $\tau_1 \approx 3$ ps and $\tau_2 \approx 1.3$ ns (Fig. S15, see SI), indicating that the presence of AR-CQDs in AR-CQDs/g-C_3N_5 at this excitation wavelength neither significantly alters the intrinsic exciton relaxation nor allows for interfacial electron transfer within the ultrafast timescale probed here. At 480 nm, TA spectra and kinetics of AR-CQDs/g-C_3N_5 again track to those of g-C_3N_5 with two characteristic time constants of $\tau_1 \approx 3$ ps and $\tau_2 \approx 50$ ps (Fig. S16, see SI), consistent with the low absorption cross-section of AR-CQDs, leading to no ultrafast interfacial electron transfer. A full account of the 320 and 480 nm measurements – including TA spectra, kinetics, and global fits for AR-CQDs/g-C_3N_5, g-C_3N_5, and AR-CQDs, and a comparative analysis of the 320, 400, and 480 nm TA datasets, highlighting the distinct interfacial response at 400 nm – is provided in the SI (Note S2 and Fig. S14–S16, and Table S5, see SI).

Although 320 nm excitation provides a larger thermodynamic driving force, it does not cause appreciable charge separation in AR-CQDs/g-C_3N_5. We ascribed this to the spatial localization of the electronic excitation within the AR-CQDs. Excitation at 320 nm generates excitons deeper within the bulk of g-C_3N_5, *i.e.*, distant from the heterointerface. These localized excitons have a short diffusion length, which hinders their migration to the AR-CQDs interface within the ultrafast timescale of charge transfer. Instead, such high-energy excitons undergo ultrafast internal conversion into energetically lower states before interfacial electron injection can occur. On the other hand, 400-nm excitation, despite the lower driving force for electron transfer, populates band-edge or shallow trap states near the interface of the AR-CQD and, hence, enables efficient oxidative quenching by charge transfer to the g-C_3N_5 ($\tau \approx 1.8$ ps). This process is likely facilitated by the surface amino functionalities of the AR-CQDs introduced during synthesis, which favorably align the electronic states at the interface and increase electronic coupling between AR-CQDs and g-C_3N_5. At 480 nm, insufficient AR-CQDs excitation precludes the same pathway.

Similar state-selective charge transfer has been reported in other QD heterojunctions: Tvrdy *et al.* reported that UV-excited CdSe QDs did not inject hot electrons into metal oxides, as the hot carriers rapidly relax to the band-edge prior to transfer.[71] Zhang *et al.* demonstrated excitation-wavelength-dependent funneling from core to trap states in CdSe QDs, where lower-energy excitation preferentially populated trap states involved in interfacial transfer.[72] In a contrasting case, Sayyad *et al.* observed that core-state excitation in differently emitting carbon dots promoted more efficient electron injection into an acceptor than surface-state excitation, due to the presence of electron-trapping functional groups.[73] Grimaldi *et al.* showed

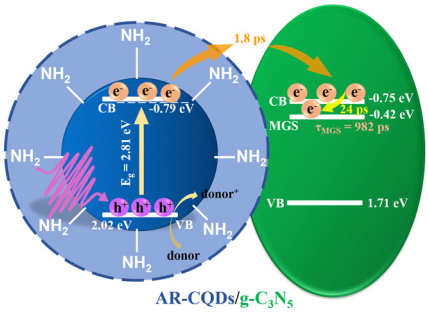

Fig. 8 Proposed interfacial charge-transfer model for AR-CQDs/g-C_3N_5 under 400 nm excitation: photoexcitation of AR-CQDs generates electron–hole pairs, followed by ultrafast electron injection from AR-CQDs into the conduction band of g-C_3N_5 within 1.8 ps. The injected electrons subsequently relax into N_{2C}-vacancy-derived mid-gap states (MGSs) on a 24 ps timescale. The trapped-electron population in these MGSs exhibits a lifetime of 982 ps, providing a long-lived electron reservoir for interfacial redox reactions. The complementary holes remain on the AR-CQDs side and are consumed by the sacrificial donor, suppressing recombination.

that higher energy excitations in PbSe–CdSe QD heterojunctions enabled faster and more efficient hot electron injection across QD interfaces, provided that the transfer outcompeted thermalization.[74] Thus, our results add to the notion of a very system-dependent excitation wavelength-dependent charge transfer mechanism in QD-heterostructures, and the work emphasizes the importance of state localization, energy level alignment, and trap dynamics in determining the photocatalytic efficiency of such heterostructures.

Taken together, steady-state spectroscopy (UV-vis, DRS, PDS, and PL), photocurrent and EIS, and fs-TAS establish the mechanistic role of the defect-interface synergy in AR-CQDs/g-C_3N_5. AR-CQDs anchoring creates N_{2C} vacancy derived MGSs in AR-CQDs/g-C_3N_5, enhances interfacial coupling, and critically enables rapid electron injection from AR-CQDs to g-C_3N_5 at 400 nm, with long-lived electron storage in MGSs. The synergy between interfacial injection and defect-assisted charge storage therefore increases the steady-state population of long-lived electrons available for CO_2 photoreduction and H_2 evolution, providing a mechanistic rational for the improved photocatalytic activity of AR-CQDs/g-C_3N_5. This is precisely the excitation window relevant to our catalytic conditions, and it rationalizes the superior CO_2 photoreduction to CH_3CHO and H_2 productivities in AR-CQDs/g-C_3N_5. Based on our results and previous studies,[75] we propose an interfacial charge-transfer model for AR-CQDs/g-C_3N_5 under optimized conditions and summarize the operative charge-transfer pathway in Fig. 8. Upon excitation at 400 nm, a significant fraction of photons is absorbed by the AR-CQDs. The excitation primarily populates energy levels near the CB edge of AR-CQDs (−0.79 eV *vs.* NHE), including surface-associated emissive states formed by nitrogen-rich functional groups. Favourable alignment of these energy levels with the CB of g-C_3N_5 (−0.75 eV *vs.* NHE, as reported previously[44]) drives ultrafast oxidative quenching of the AR-CQDs and electron injection into g-C_3N_5 within 1.8 ps, evidenced by GSB blue-shift and ESA growth in fs-TA, indicative of enhanced electron density populating the CB and shallow trap states in g-C_3N_5. Injected electrons then relax into MGSs (−0.42 eV *vs.* NHE), associated primarily with N_{2C} vacancies, on a *ca.* 24 ps timescale and persist for a comparably long timescale of *ca.* 1 ns, providing a reservoir for interfacial redox. The vacancies thus act as electron trapping and relay sites, that facilitate charge separation and suppress recombination – consistent with enhanced transient photocurrent, and lower charge-transfer resistance in EIS. The complementary holes remain on the AR-CQDs side and are quenched by the sacrificial donor.

As a result of interfacial electron transfer and vacancy-assisted electron storage, AR-CQDs/g-C_3N_5 sustains a higher steady-state population of long-lived electrons at the g-C_3N_5 surface, increasing the probability of multi-electron CO_2 conversion under illumination. At this stage, the present dataset does not allow unambiguous assignment of the CO_2 adsorption sites, surface-bound intermediates, or the C–C coupling pathway leading to CH_3CHO. Nevertheless, the enhanced activity and selectivity are consistent with the improved charge separation, prolonged carrier lifetimes, and increased interfacial electron availability demonstrated by fs-TAS, transient photocurrent, and EIS. Photogenerated holes are consumed by the sacrificial donor, thereby suppressing charge recombination. This defect-interface synergy—ultrafast electron injection followed by mid-gap-state-assisted charge storage—provides a mechanistic rationale for the boosted CO_2 reduction and H_2 evolution performance of AR-CQDs/g-C_3N_5.

Conclusions

We reported a metal-free 0D/2D heterojunction photocatalyst in form of AR-CQDs/g-C_3N_5, that couples AR-CQDs with nitrogen-rich g-C_3N_5 while creating N_{2C} vacancy MGSs. This defect-interface engineering leads to a significantly enhanced photocatalytic activity of AR-CQDs/g-C_3N_5 for both CO_2 reduction and H_2 evolution. Under blue-light excitation, AR-CQDs/g-C_3N_5 achieved 7-fold higher CH_3CHO production rates than g-C_3N_5 and 48-fold higher than traditional g-C_3N_4, along with H_2 evolution rates increasing by around 3.4-fold and 15-fold, respectively, while maintaining excellent stability over multiple cycles without structural degradation. AR-CQDs/g-C_3N_5 further yields favorable band alignment and enhanced interfacial coupling, verified by steady-state optics, ultrafast photophysics, and electrochemistry. Femtosecond TA reveals a state-selective pathway at 400 nm, including ultrafast electron injection from photoexcited AR-CQDs to g-C_3N_5 (1.8 ps), followed by trapping in vacancy-derived MGSs (24 ps), and sub-ns persistence (982 ps) – a sequence that decouples charges and supplies long-lived electrons for surface reactions. These results directly resolve the proposed defect-interface synergy, such as, the heterointerface enables ultrafast electron injection from photoexcited AR-CQDs to g-C_3N_5, whereas the vacancy-derived MGSs trap and retain the injected electrons on longer timescales,

thereby prolonging charge separation and increasing the electron population available for photocatalysis. In contrast, 320 nm excitation relaxes within g-C_3N_5 before reaching the interface and 480 nm weakly excites the AR-CQDs – neither condition produces resolvable interfacial injection. Thus, efficient charge separation is excitation-window dependent, governed by state localization rather than driving force alone. Together, these results establish a direct link between ultrafast interfacial electron transfer and observed photocatalytic performance. Finally, this work delivers a novel approach for developing visible-light-driven, metal-free, and sustainable heterogeneous carbon-nitride heterojunctions *via* engineered nitrogen vacancies with targeted interfacial states and exciting within the CQD band-edge window to efficiently suppress charge carrier recombination, generate abundant active sites, and enhance photogenerated electron dynamics, paving the way for advanced solar-to-chemical energy conversion technologies.

Author contributions

Dr Pratibha Saini: conceptualization, methodology, material synthesis, photocatalytic tests, characterization, data curation, writing – original draft, supervision. Arindam Konar: conceptualization, methodology, ultrafast spectroscopy experiments, data curation, writing – original draft. Ahmed Mansour: material preparation, photocatalytic tests, GC analysis. Dr Sarah Jasmin Finkelmeyer and Dr Martin Presselt: photothermal deflection spectroscopy (PDS) characterization and analysis, Dr Desirée Leistenschneider and Marius Hermesdorf: XPS and gas physisorption characterization and analysis. Prof. Dr Martin Oschatz: supervision, writing – review & editing. Prof. Dr Benjamin Dietzek-Ivanšić: investigation, supervision, writing – review & editing, validation, funding acquisition.

Conflicts of interest

There are no conflicts to declare.

Data availability

The data supporting the findings of this study are available within the article and its supplementary information (SI). Supplementary information: this includes synthesis processes, structural and spectroscopic characterization methods, photocatalytic tests, and detailed steady-state and ultrafast spectroscopy data and discussion. See DOI: https://doi.org/10.1039/d5ey00355e.

Acknowledgements

P. S. and A. K. contributed equally to this work. This work was funded by the Deutsche Forschungsgemeinschaft, DFG *via* TRR CataLight, projects B06, B09, and B10, 364549901. P. S. extends her gratitude to the Walter Benjamin Programme (DFG, project number: 530742479) and the ProChanceCareer Programme for their financial support. P. S. would also like to thank Andrea Dellith and Dr Jan Dellith (Leibniz Institute of Photonic Technology, Jena) for their assistance with SEM, EDX, and TEM measurements and Dr Lingli Ni for her assistance during the material synthesis. M. H. and D. L. acknowledge the Fonds der Chemischen Industrie for financial support through the Liebig fellowship. D. L. thanks the Carl-Zeiss-Stiftung for financial support of the project ReAlBatt (P2022-04-046) within the Nexus program.

Notes and references

1 X. Wang, K. Maeda, A. Thomas, K. Takanabe, G. Xin, J. M. Carlsson, K. Domen and M. Antonietti, *Nat. Mater.*, 2009, **8**, 76.
2 J. Lin, Z. Pan and X. Wang, *ACS Sustainable Chem. Eng.*, 2014, **2**, 353.
3 P. Saini, K. Kumar, S. Saini, M. Sethi, P. Meena, A. Gurjar, W. Weigand and V. Parewa, *J. Energy Chem.*, 2025, **105**, 525.
4 S. Fang, M. Rahaman, J. Bharti, E. Reisner, M. Robert, G. A. Ozin and Y. H. Hu, *Nat. Rev. Methods Primers*, 2023, **3**, 61.
5 M. M. Kandy, A. Rajeev K and M. Sankaralingam, *Sustainable Energy Fuels*, 2021, **5**, 12.
6 K. Kumar, P. Saini, M. Sethi, S. Saini, A. Gurjar, A. Konar, B. Dietzek-Ivanšić, W. Weigand and V. Parewa, *ACS Appl. Mater. Interfaces*, 2024, **16**, 43498.
7 A. Konar, J. Liessem, C. Im, M. M. Elnagar, D. Mitoraj, P. Saini, I. Krivtsov, S. J. Finkelmeyer, J. Griebel, M. Presselt, T. Jacob, R. Beranek and B. Dietzek-Ivanšić, *Adv. Sci.*, 2025, **12**, e09312.
8 I. Krivtsov, D. Mitoraj, C. Adler, M. Ilkaeva, M. Sardo, L. Mafra, C. Neumann, A. Turchanin, C. Li, B. Dietzek, R. Leiter, J. Biskupek, U. Kaiser, C. Im, B. Kirchhoff, T. Jacob and R. Beranek, *Angew. Chem., Int. Ed.*, 2020, **59**, 487.
9 C. Adler, I. Krivtsov, D. Mitoraj, L. dos Santos-Gómez, S. García-Granda, C. Neumann, J. Kund, C. Kranz, B. Mizaikoff, A. Turchanin and R. Beranek, *ChemSusChem*, 2021, **14**, 2170.
10 L. Ni, E. Troschke, H. Vorwerk, S. S. Avarvand, A. Stihl, N. Brezhneva, M. Hermesdorf, D. Leistenschneider, F. H. Schacher, J. Schneidewind and M. Oschatz, *Adv. Funct. Mater.*, 2025, e04107.
11 A. Dandia, S. L. Gupta, P. Saini, R. Sharma, S. Meena and V. Parewa, *Curr. Res. Green Sustainable Chem.*, 2020, **3**, 100039.
12 J. Liu, H. Wang and M. Antonietti, *Chem. Soc. Rev.*, 2016, **45**, 2308.
13 J. Zhu, P. Xiao, H. Li and S. A. C. Carabineiro, *ACS Appl. Mater. Interfaces*, 2014, **6**, 16449.
14 J. Yang, H. Wang, L. Jiang, H. Yu, Y. Zhao, H. Chen, X. Yuan, J. Liang, H. Li and Z. Wu, *Chem. Eng. J.*, 2022, **427**, 130991.
15 G. P. Mane, S. N. Talapaneni, K. S. Lakhi, H. Ilbeygi, U. Ravon, K. Al-Bahily, T. Mori, D.-H. Park and A. Vinu, *Angew. Chem., Int. Ed.*, 2017, **56**, 8481.

16 P. Kumar, E. Vahidzadeh, U. K. Thakur, P. Kar, K. M. Alam, A. Goswami, N. Mahdi, K. Cui, G. M. Bernard, V. K. Michaelis and K. Shankar, *J. Am. Chem. Soc.*, 2019, **141**, 5415.
17 H.-T. Vuong, D.-V. Nguyen, L. P. Phuong, P. P. D. Minh, B. N. Ho and H. A. Nguyen, *Carbon Neutralization*, 2023, **2**, 425.
18 S. Tharuman, R. Karthikeyani, S.-M. Chen, V. Balakumar, N. Nataraj and V. Sasirekha, *J. Environ. Chem. Eng.*, 2023, **11**, 111376.
19 J. Liu, S. Wang, C. Zhao and J. Zheng, *Nanomaterials*, 2023, **13**, 499.
20 C. I. Sathish, S. Premkumar, X. Chu, X. Yu, M. B. H. Breese, M. Al-Abri, A. H. Al-Muhtaseb, A. Karakoti, J. Yi and A. Vinu, *Angew. Chem.*, 2021, **133**, 21412.
21 S. Qin, L. Huang, Y. Zhang, T. Zhang, M. Tian and J. Jiang, *Sci. Rep.*, 2025, **15**, 787.
22 G. Li, G. Zeng, Z. Chen, J. Hong, X. Ji, Z. Lan, X. Tan, M. Li, X. Hu and C. Tang, *Nanomaterials*, 2022, **12**, 2701.
23 L. Huang, Z. Liu, W. Chen, D. Cao and A. Zheng, *J. Mater. Chem. A*, 2018, **6**, 7168.
24 S. Li, M. Cai, Y. Liu, J. Zhang, C. Wang, S. Zang, Y. Li, P. Zhang and X. Li, *Inorg. Chem. Front.*, 2022, **9**, 2479.
25 S. Vadivel, M. Fujii and S. Rajendran, *Environ. Res.*, 2022, **213**, 113736.
26 Y. Chen and X. Bai, *Catalysts*, 2020, **10**, 142.
27 H. Lee, H. C. Leventis, S.-J. Moon, P. Chen, S. Ito, S. A. Haque, T. Torres, F. Nüesch, T. Geiger, S. M. Zakeeruddin, M. Grätzel and Md. K. Nazeeruddin, *Adv. Funct. Mater.*, 2009, **19**, 2735.
28 P. V. Kamat, K. Tvrdy, D. R. Baker and E. J. Radich, *Chem. Rev.*, 2010, **110**, 6664.
29 A. Dandia, P. Saini, M. Sethi, K. Kumar, S. Saini, S. Meena, S. Meena and V. Parewa, *Catal. Rev.*, 2023, **65**, 874.
30 X.-D. Mai, T. T. K. Chi, T.-C. Nguyen and V.-T. Ta, *Mater. Lett.*, 2020, **268**, 127595.
31 R. Wang, K.-Q. Lu, Z.-R. Tang and Y.-J. Xu, *J. Mater. Chem. A*, 2017, **5**, 3717.
32 P. Devi, S. Saini and K.-H. Kim, *Biosens. Bioelectron.*, 2019, **141**, 111158.
33 F. Wang, Y. Wang, Y. Wu, D. Wei, L. Li, Q. Zhang, H. Liu, Y. Liu, W. Lv and G. Liu, *Environ. Sci.: Nano*, 2019, **6**, 2565.
34 Z. Xu, W. Shi, Y. Shi, H. Sun, L. Li, F. Guo and H. Wen, *Appl. Surf. Sci.*, 2022, **595**, 153482.
35 A. S. Rasal, S. Yadav, A. Yadav, A. A. Kashale, S. T. Manjunatha, A. Altaee and J.-Y. Chang, *ACS Appl. Nano Mater.*, 2021, **4**, 6515.
36 Y. Chen, M. Cheng, C. Lai, Z. Wei, G. Zhang, L. Li, C. Tang, L. Du, G. Wang and H. Liu, *Small*, 2023, **19**, 2205902.
37 J. Zhang, Z. Li, J. He, H. Tao, M. Chen, Y. Zhou and M. Zhu, *ACS Catal.*, 2023, **13**, 785.
38 Y. Shen, X. Du, Y. Shi, L. J. N. Kuate, Z. Chen, C. Zhu, L. Tan, F. Guo, S. Li and W. Shi, *Adv. Powder Mater.*, 2024, **3**, 100202.
39 E. Cui, Y. Lu, Z. Li, J. Sang, Z. Wang, M. Xie, X. Yang, J. Cao and Y. Zhang, *Appl. Catal., B*, 2024, **347**, 123806.
40 J. Zhang, Z. Li, B. Liu, M. Chen, Y. Zhou and M. Zhu, *Appl. Catal., B*, 2023, **328**, 122522.
41 X. Wang, K. Wu, W. Cao, K. Rui, W. Wang, R. Zhu, J. Zhu and Z. Yan, *Adv. Mater. Interfaces*, 2023, **10**, 2201627.
42 S. Saini, P. Saini, K. Kumar, M. Sethi, P. Meena, A. Gurjar, A. Dandia, T. Dhuria and V. Parewa, *ACS Appl. Mater. Interfaces*, 2023, **15**, 49083.
43 S. Saini, K. Kumar, P. Saini, M. Sethi, P. Meena, A. Dandia, W. Weigand and V. Parewa, *ACS Appl. Mater. Interfaces*, 2024, **16**, 46200.
44 S. Meena, M. Sethi, S. Saini, K. Kumar, P. Saini, S. Meena, S. Kashyap, M. Yadav, M. L. Meena, A. Dandia, N. K. Nirmal and V. Parewa, *J. Colloid Interface Sci.*, 2024, **660**, 756.
45 Z. Li, Y. Zhou, Y. Zhou, K. Wang, Y. Yun, S. Chen, W. Jiao, L. Chen, B. Zou and M. Zhu, *Nat. Commun.*, 2023, **14**, 5742.
46 A. Yuan, H. Lei, F. Xi, J. Liu, L. Qin, Z. Chen and X. Dong, *J. Colloid Interface Sci.*, 2019, **548**, 56.
47 C. Fan, J. Miao, G. Xu, J. Liu, J. Lv and Y. Wu, *RSC Adv.*, 2017, **7**, 37185.
48 X. Bai, L. Wang, R. Zong and Y. Zhu, *J. Phys. Chem. C*, 2013, **117**, 9952.
49 (*a*) H. Zhang, Y. Cao, Z. Li, Y. Gao, L. Shangguan, J. Sun, L. Lang and W. Lei, *J. Catal.*, 2023, **417**, 360; (*b*) D. Gong, J. Guo, F. Wang, J. Zhang, S. Song, B. Feng, X. Zhang and W. Zhang, *Food Chem.*, 2023, **425**, 136470.
50 I. Y. Kim, S. Kim, X. Jin, S. Premkumar, G. Chandra, N.-S. Lee, G. P. Mane, S.-J. Hwang, S. Umapathy and A. Vinu, *Angew. Chem.*, 2018, **130**, 17381.
51 C. Hu, Y.-H. Lin, M. Yoshida and S. Ashimura, *ACS Appl. Mater. Interfaces*, 2021, **13**, 24907.
52 H. Wang, M. Li, Q. Lu, Y. Cen, Y. Zhang and S. Yao, *ACS Sustainable Chem. Eng.*, 2019, **7**, 625.
53 P. Niu, L.-C. Yin, Y.-Q. Yang, G. Liu and H.-M. Cheng, *Adv. Mater.*, 2014, **26**, 8046.
54 H. Feng, Q. Guo, Y. Xu, T. Chen, Y. Zhou, Y. Wang, M. Wang and D. Shen, *ChemSusChem*, 2018, **11**, 4256.
55 Y. Zheng, Y. Luo, Q. Ruan, J. Yu, X. Guo, W. Zhang, H. Xie, Z. Zhang, J. Zhao and Y. Huang, *J. Colloid Interface Sci.*, 2022, **609**, 75.
56 T. Huang, S. Pan, L. Shi, A. Yu, X. Wang and Y. Fu, *Nanoscale*, 2020, **12**, 1833.
57 M. K. T. Chee, C.-C. Er, J.-Y. Tang, L.-L. Tan, W. S. Chang and S.-P. Chai, *Appl. Surf. Sci.*, 2020, **529**, 146600.
58 Y. Wang, T. N. Pham, Y. Tian, Y. Morikawa and L. Yan, *J. Colloid Interface Sci.*, 2021, **585**, 740.
59 K. Kong, H. Zhong, F. Zhang, H. Lv, X. Li and R. Wang, *Adv. Funct. Mater.*, 2025, **35**, 2417109.
60 W. Kwon, S. Do, J.-H. Kim, M. S. Jeong and S.-W. Rhee, *Sci. Rep.*, 2015, **5**, 12604.
61 H. Shabbir, E. Csapó and M. Wojnicki, *Inorganics*, 2023, **11**, 262.
62 Y. Han, L. Liccardo, E. Moretti, H. Zhao and A. Vomiero, *J. Mater. Chem. C*, 2022, **10**, 11827.
63 Y. Dong, R. Wang, H. Li, J. Shao, Y. Chi, X. Lin and G. Chen, *Carbon*, 2012, **50**, 2810.

64 Y.-P. Sun, B. Zhou, Y. Lin, W. Wang, K. A. S. Fernando, P. Pathak, M. J. Meziani, B. A. Harruff, X. Wang, H. Wang, P. G. Luo, H. Yang, M. E. Kose, B. Chen, L. M. Veca and S.-Y. Xie, *J. Am. Chem. Soc.*, 2006, **128**, 7756.
65 H. Li, X. He, Z. Kang, H. Huang, Y. Liu, J. Liu, S. Lian, C. H. A. Tsang, X. Yang and S.-T. Lee, *Angew. Chem., Int. Ed.*, 2010, **49**, 4430.
66 S. Zhu, Q. Meng, L. Wang, J. Zhang, Y. Song, H. Jin, K. Zhang, H. Sun, H. Wang and B. Yang, *Angew. Chem., Int. Ed.*, 2013, **52**, 3953.
67 R. Godin, Y. Wang, M. A. Zwijnenburg, J. Tang and J. R. Durrant, *J. Am. Chem. Soc.*, 2017, **139**, 5216.
68 W. Wang, X. Bai, Q. Ci, L. Du, X. Ren and D. L. Phillips, *Adv. Funct. Mater.*, 2021, **31**, 2103978.
69 H. Sun, K. Wei, D. Wu, Z. Jiang, H. Zhao, T. Wang, Q. Zhang and P. K. Wong, *Appl. Catal., B*, 2020, **264**, 118480.
70 X. Wen, P. Yu, Y.-R. Toh, X. Hao and J. Tang, *Adv. Opt. Mater.*, 2013, **1**, 173.
71 K. Tvrdy, P. A. Frantsuzov and P. V. Kamat, *Proc. Natl. Acad. Sci. U. S. A.*, 2010, **108**, 29.
72 L. Zhang, Q. Xu, M. Liu, L. Kong, M. Jiao, H. Mu, D. Wang, H. Wang, J. Chen and C. Yang, *Nanoscale Res. Lett.*, 2017, **12**, 222.
73 U. S. Sayyad, H. Bhatt, H. N. Ghosh and S. Mondal, *Nanoscale*, 2024, **16**, 8143.
74 G. Grimaldi, R. W. Crisp, S. ten Brinck, F. Zapata, M. van Ouwendorp, N. Renaud, N. Kirkwood, W. H. Evers, S. Kinge, I. Infante, L. D. A. Siebbeles and A. J. Houtepen, *Nat. Commun.*, 2018, **9**, 2310.
75 X. Qian, W. Yang, S. Gao, J. Xiao, S. Basu, A. Yoshimura, Y. Shi, V. Meunier and Q. Li, *ACS Appl. Mater. Interfaces*, 2020, **12**, 55982.